



Adhesion and stiffness matching in epoxyvitrimers/strain sensor fiber laminates

Jakob Langenbach, Camille Bakkali-Hassani, Quentin-Arthur Poutrel,
Antonia Georgopoulou, Frank Clemens, François Tournilhac, Sophie Norvez

► To cite this version:

Jakob Langenbach, Camille Bakkali-Hassani, Quentin-Arthur Poutrel, Antonia Georgopoulou, Frank Clemens, et al.. Adhesion and stiffness matching in epoxyvitrimers/strain sensor fiber laminates. ACS Applied Polymer Materials, 2022, 4 (2), pp.1264-1275. 10.1021/acsapm.1c01648 . hal-03624829

HAL Id: hal-03624829

<https://hal.science/hal-03624829>

Submitted on 30 Mar 2022

HAL is a multi-disciplinary open access archive for the deposit and dissemination of scientific research documents, whether they are published or not. The documents may come from teaching and research institutions in France or abroad, or from public or private research centers.

L'archive ouverte pluridisciplinaire **HAL**, est destinée au dépôt et à la diffusion de documents scientifiques de niveau recherche, publiés ou non, émanant des établissements d'enseignement et de recherche français ou étrangers, des laboratoires publics ou privés.

Adhesion and stiffness matching in epoxy-vitrimers/strain sensor fiber laminates

Jakob Langenbach¹, Camille Bakkali-Hassani¹, Quentin-Arthur Poutrel¹, Antonia Georgopoulou^{2,3}, Frank Clemens², François Tournilhac¹, Sophie Norvez^{1*}

¹ Molecular, Macromolecular Chemistry, and Materials, ESPCI Paris, PSL University, CNRS UMR7167, 75005 Paris, France

² Department of Functional Materials, Empa - Swiss Federal Laboratories for Materials Science and Technology, Überlandstrasse 129, 8600 Dübendorf, Switzerland

³ Brubotics, Vrije Universiteit Brussel (VUB), Pleinlaan 2, B-1050 Brussels, Belgium

* Author for correspondence: sophie.norvez@espci.fr

Abstract

Hybrid networks, *i.e.* including physical and chemical crosslinks, were synthesized from bio-sourced fatty acid fragments, linked to each other by a controlled number of non-exchangeable ether bonds, exchangeable ester bonds and non-covalent hydrogen bonds. The mechanical properties of these networks are tuned by the ratio di- versus tetra-epoxide, and the stoichiometry acid/epoxy. Creep tests and insolubility demonstrated the vitrimer or vitrimer-like nature of the resulting materials. The thermo-stimulated welding ability of the materials was exploited to incorporate strain sensors by embedding electrically conductive fibers into the rubbery vitrimer matrix. The efficiency of the welding procedure at moderate temperatures (80 °C) and the tunability of mechanical properties are both attractive assets for effective incorporation of thermodegradable conductive fibers while preserving their mechanical and electrical integrity. Mechanical and electrical behavior of the sensor composites were simultaneously tested, either in quasi-static or in cyclic tensile experiments, at room temperature and at distance from the T_g of the matrices. The study emphasizes the importance of matching Young's moduli of components in composite samples, which is strongly temperature-dependent.

Keywords: soft robotics, elastomeric vitrimer, electrically conductive composites, matrix-sensor fiber laminates, stiffness matching

Introduction

Soft robotics is an emergent branch of robotics, which involves incorporation of elastomeric elements. Addition of soft materials into robotic devices allows better flexibility and adaptability to the environment than when robots are made of hard and rigid components.¹ These features make soft robots a promising technology for biomedical,^{2,3} food industry⁴ or space⁵ applications, insofar mechanical impedance of the robotic fingers could match those of the objects manipulated. However, transfer from academic research to industry still provides some challenges.⁶ In particular, the loss of the robot functionality is a major concern after material damages, intrinsically favoured by the soft nature of the components.⁷ To address this issue, the use of self-healing (SH) elastomers figures among available solutions.⁸

SH ability has been demonstrated in diverse elastomers made of physical or chemical networks. SH physical networks may be obtained by association of macromolecules through small glassy or crystalline domains, ionic aggregates or hydrogen bonds. SH elastomers based solely on small molecules linked by hydrogen bonds have even been described.⁹ SH chemical networks may be built from dynamic covalent chemistry as well. In all cases, a trade-off between SH ability and mechanical properties is unavoidable.¹⁰ The supramolecular rubbers exhibit creep under load or stress as the strength of the exchangeable bonds is low. Dynamic covalent networks with reversible links lose their integrity through dissociation of cross-linkers at high temperature. In dissociative systems, either non-covalent or covalent, the cross-link density depends on the equilibrium between the associated and dissociated bonds, as bonds are continuously broken and re-formed, and this equilibrium shifts to dissociation when temperature is elevated. To face the dilemma, a strategy combining two reversible cross-linkers working at different time scales, hydrogen bonds and Diels-Alder adducts, has been proposed.¹¹ Slowly exchanging Diels-Alder cross-linkers limited creep at room temperature while faster exchange under heat allowed reshaping. Improvement of the mechanical performances of a covalent SH material using sacrificial hydrogen bonds grafts has also been considered.¹² Still a dissociative mechanism cannot maintain shape at high temperature.

In contrast, systems using an associative mechanism may afford retention of the crosslink density, as in this case a bond cleavage occurs simultaneously with the formation of a new cross-link. This strategy was first worked out by Leibler and coworkers who named their materials vitrimers.^{13–15} Prototypes of vitrimers were based on exchanges by transesterification in acid/epoxy networks; since then, numerous other inventive chemistries have been investigated.^{16–24} In vitrimer systems, the temperature increase accelerates the exchange rate of covalent bonds, while the total number of crosslinks remains constant.

Reprocessing and full recycling have been subsequently demonstrated in such systems. Dissociative mechanism takes profit of local concentration of reactive species at the wound location, facilitating healing through bridging interfaces, but full reprocessing is not accessible without extensive loss of integrity. A strategy to provide integrity to reparable soft materials, deformable under load or heat, consists in introducing intentionally some permanent covalent links.^{25–27} Poutrel *et al.* have recently shown that a slight off-stoichiometry in the ratio acid/epoxy greatly improved the mechanical properties of the resultant resin.^{26–27} From this point of view, even side reactions giving rise to permanent crosslinks may reveal as auxiliaries for self-healing behavior. The small amount of permanent network improves mechanical properties, yet allowing repeated repair or at least welding. Such materials have been referred to as being vitrimer-like.^{26–30}

To achieve automated operations and to detect a material damage (and possibly start a healing process), a soft robot must be equipped with a sensing system such as strain sensors.^{31–33} To produce stretchable electronics with self-healing properties, two strategies have been described: (i) combining self-healing elastomers with carbon black fillers,³⁴ and (ii) embedding sensor fibers in an elastomer matrix.³⁵ The first strategy yields to composites with significantly higher stiffness and shorter range of deformation than the second one.^{36,37} The second strategy limits the undesired matrix stiffening but requires a good integration of the sensor fibers in the elastomer matrix.^{36–38}

In this work, epoxy-acid vitrimer or vitrimer-like networks with tunable mechanical properties are prepared as matrices for strain sensor integration. Four different vitrimer materials incorporating reversible hydrogen bonds, exchangeable ester bonds and small amount of permanent ether bonds are prepared in a straightforward two-step synthesis, and their mechanical properties are quantified. Their thermostimulated self-healing capability is exploited to devise a sandwich-welding procedure where a carbon/polymer composite fiber is embedded between two elastomer strips. The electrical and mechanical behaviors of the resulting sensor fiber composite (SFC) are investigated simultaneously in two different situations: (i) at large (> 100 %) deformation using quasi-static tensile testing conditions and (ii) at 20 % applied deformation, using dynamic cycling conditions. Dissimilar behavior observed at room temperature and at 50 °C is analysed in terms of difference in the Young's moduli of fiber and matrix.

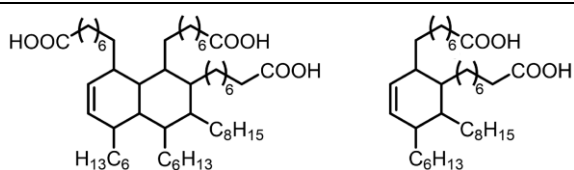
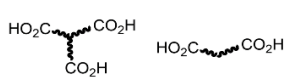
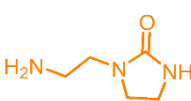

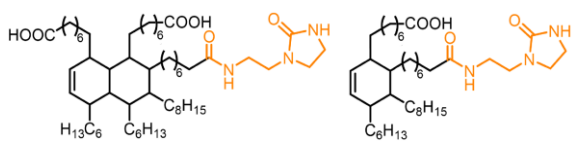
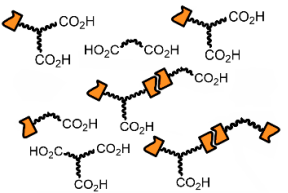
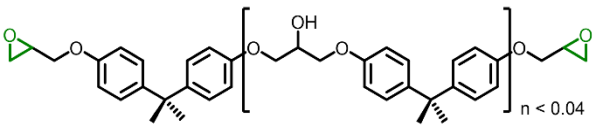

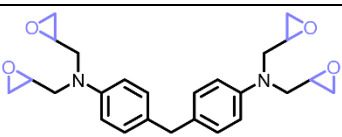
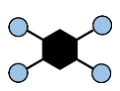
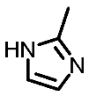
1. Experimental Section

1.1 Materials

Pripol 1040 (vegetable fatty acid oil) with dicarboxylic (23 wt %) and tricarboxylic (77 wt %) acids were obtained from Croda. 2-Aminoethylimidazolidone (UDETA) was kindly provided

by Arkema. A bifunctional diglycidyl ether of bisphenol A (DGEBA, DER332) and a tetrafunctional 4,4'-methylene-bis (*N,N*-diglycidylaniline) (TGMDA) were purchased from Sigma-Aldrich. 2-Methylimidazole (2-MI) supplied from Fluka was used as crosslinking catalyst. Pripol 1040, DGEBA, TGMDA, and 2-MI were used as received. UDETA with an initial purity of 83 wt % (95 mol %) was distilled under vacuum at 160 °C and recrystallized from a toluene/chloroform (mass ratio 80/20) mixture before use. Detailed formulae may be found in Table 1.

Table 1. Molecular structure, scheme, and name/role of all used reactants.

Component	Scheme	Name/Role
 <p>Mixture (trimer 77 wt % and dimer 23 wt %)</p>		Fatty acid/ precursor of supramolecular prepolymer SP50
		UDETA/ hydrogen bonding unit
 <p>Partially functionalized trimers and dimers</p>		SP50/ Supramolecular prepolymer
		DGEBA/ Bi-functional epoxy cross-linker
		TGMDA/ Tetra-functional epoxy cross-linker
	None	2-MI/ Catalyst and initiator

1.2 Supramolecular Prepolymer liquid precursor (SP50) preparation

The liquid precursor, SP50 with a target conversion of 50 mol % of acid into amide, was synthesized as already reported by reacting Pripol 1040 and UDETA as detailed in the Supporting Information.³⁹

1.3 Hybrid network synthesis

The hybrid networks are denoted as $x\text{D}-(100-x)\text{T}_n\text{epoxy}$, where x is the mol % epoxy ($x = 0$ or 75), n the excess mol % epoxy ($n = 0, 5, 10$ or 50), D and T represent DGEBA and TGMMA, respectively. Flat sheets of hybrid networks were obtained according to the procedure detailed in the Supporting Information. Table S1 summarizes the chemical composition of the five hybrid networks synthesized.

1.4 Sensor fiber synthesis

For the piezoresistive sensor composite, a styrene-based triblock copolymer by Kraiburg TPE (Waldkraiburg, Germany) was combined with carbon black obtained from TIMCAL (Bodio, Switzerland). The two components were mixed in a 1:1 mass ratio (50 wt % carbon black), using torque rheometer HAAKE PolyLab Rheomix 600 from Thermofisher (Karlsruhe, Germany). Sensor fibers with a diameter of 0.3 mm were extruded using a capillary rheometer RH7 from NETZSCH (Selb, Germany). The temperature used for the mixing and the extrusion was 190 °C. The sensor fiber fabrication and properties have been reported elsewhere.⁴⁰ The sensing mechanism is based on the rotation of the conductive particles, as well as on tunneling and hopping, and not on cracks formation as proposed by Liu and Shen.^{41,42}

1.5 Integration of sensor fibers into vitrimer matrices

The sensor fiber was pre-stretched to 50 % strain for one minute to ensure reproducible sensing properties. The ends of the fiber were connected to a thin metal wire with cable end sleeves and conductive glue. Dog-bone shaped specimen with a total length of 13 cm (gauge length 25 mm) were punched from the cured sheets. These samples were stored in an oven (22 °C, 30 % relative humidity) for several days to equilibrate the material and avoid dust attachment. For welding, the sensor fiber was placed between two dog-bone shaped samples, with no additional cleaning of the connected surfaces. Sensor fiber composites (SFCs) were sandwich-welded at 80 °C for 1 h with a 1 kg weight to induce flow of the assembly. After the heating period, the temperature is reduced slowly to improve the connection between the dog-bone sheets.

1.6 Chemical analysis

¹H NMR spectroscopy, ATR-IR measurements, and solubility tests (solvent uptake, % gel) were performed as described in the Supporting Information.

1.7 Thermomechanical properties

DSC and DMA experiments were performed as described in the Supporting Information.

Creep measurements were performed in compression mode with disk-shaped specimens (diameter 12.5 mm and thickness 2 mm). Six 1 h-steps were operated every 10 °C from 110 °C to 160 °C, 45 min of 0.01 MPa stress followed by 15 min of relaxation.

1.8 Mechanical and electrical properties

Tensile tests were performed at room temperature on three different dog-bone specimens of 4 mm width, 25 mm gauge length, and 2 mm thickness. All tensile tests were done with an Instron 5900 machine with pneumatic clamps (pressure 2 bars) at a deformation rate of 25 mm.min⁻¹. The experiment was followed with a video extensometer.

The adhesion of the sensor fiber composite was tested with rectangular samples (40 mm × 9 mm × 4 mm) at T-peel tests. The crosshead speed was 10 mm.min⁻¹ or 2.5 mm.min⁻¹ and the measured force divided by the width of the sample gives rise to the peeling strength (in N.m⁻¹).

For the sensor fiber composites, the sample was clamped with pneumatic holders, the wire cables were connected to a Keithley 2400 source-measure unit (sampling rate of 10 Hz) and the resistance was measured. The crosshead speed was 25 mm.min⁻¹ for tensile until fracture and 12.5 mm.min⁻¹ for cyclic loading. All tensile tests with sensor fiber composites were done at room temperature (22 °C) and the cyclic test was repeated at 50 °C. The cyclic test was performed between 0 and 5 mm displacement, which corresponds to a 20 % strain. The relative resistance, which indicates the sensitivity of the strain sensor, is the ratio of the change in resistance ($R-R_0$) divided by the resistance at rest (R_0):

$$\text{Relative resistance} = \frac{R - R_0}{R_0} \quad (1)$$

1.9 Microscopic studies

Images in polarized light were taken through crossed polarizers after fixing a weight of 100 g (1 N) at the bottom of the dog-bone composite in vertical position to exert a constant stress. Polarizers were oriented at 45° or parallel to the stretching direction. The magnified images of the rupture spots were made using a camera installed on a Leica Wild MZ8 optical microscope.

2. Results and discussion

Our group previously designed tunable self-healing supramolecular rubbers, containing a density of chemical crosslinks, adjustable through a controlled ratio of bifunctional DGEBA and tetrafunctional TGMDA epoxy monomers.³⁹ Self-healing ability was ensured by a fixed

density of H-bonds provided by the UDETA moiety carried by the crosslinker SP50. With only 25% of tetra-epoxide for 75% di-epoxide in the formulation (75D-25T sample), the materials presented modest mechanical properties but complete recovery at room temperature after damage. With 100% tetra-epoxide (0D-100T sample), the material is much stiffer but the self-healing at room temperature is poor. In another study,²⁶ it was explored the effect of an excess of epoxy monomers on the thermomechanical properties of resins made of commercial diepoxide (Araldite) and sebacic acid. Homopolymerisation during curing of non-stoichiometric systems allowed formation of non exchangeable polyether bridges, improving mechanical properties of the resin. Off-stoichiometry [epoxy]/[COOH] thus appeared as a possible lever to improve stiffness without losing too much SH ability.

In the present work, we play on both levers to tune the thermo-mechanical properties of hybrid epoxy-acid networks. The workflow is presented in Figure 1. Firstly, the concentration of hydrogen bonding moieties is fixed by the initial feed ratio $[UDETA]_0/[COOH]_0 = 0.5$ during the preparation of the liquid precursor SP50 (see section 1.2). The ratio of 50 mol % was selected to achieve high H-bonds concentration for healability at low temperature. In a second step, the remaining COOH functions of SP50 are reacted with epoxides to form the hybrid network. Following this two-step procedure, different networks have been synthesized by (i) modifying the ratio of functional epoxy groups ($[DGEBA]/[TGMDA]$) and (ii) using an off-stoichiometry ratio $[epoxy]/[COOH] > 1$, where $[epoxy] = [DGEBA] + [TGMDA]$, targeting different compromises between static and dynamic properties.

Figure 1a illustrates the second step where the hybrid network is synthesized from the liquid precursor SP50. Depending on the stoichiometry $[epoxy]/[COOH]$, only exchangeable ester bonds are formed in addition of existing H-bonds (Figure 1b), or a few supplemental non exchangeable ether bonds are produced by anionic ring-opening polymerisation (AROP),⁴³ when epoxy functionality is introduced in excess (Figure 1c). Such a dual-curing methodology involving epoxy excess have been proved as suitable to control cure parameters like gelation time in epoxy-acid thermosets.^{43,44} Here excess of epoxy was used to improve the mechanical properties of the rather soft 75D-25T material. Samples containing n mol % epoxy excess are denoted (75D-25T_ n epoxy) in Table S1. The sample containing 50 mol % excess (75D-25T_50epoxy) was synthesized as a tool to assess the formation of ether bridges by spectroscopy.

Processing from liquid reactive mixture

a)

Casting, molding and curing

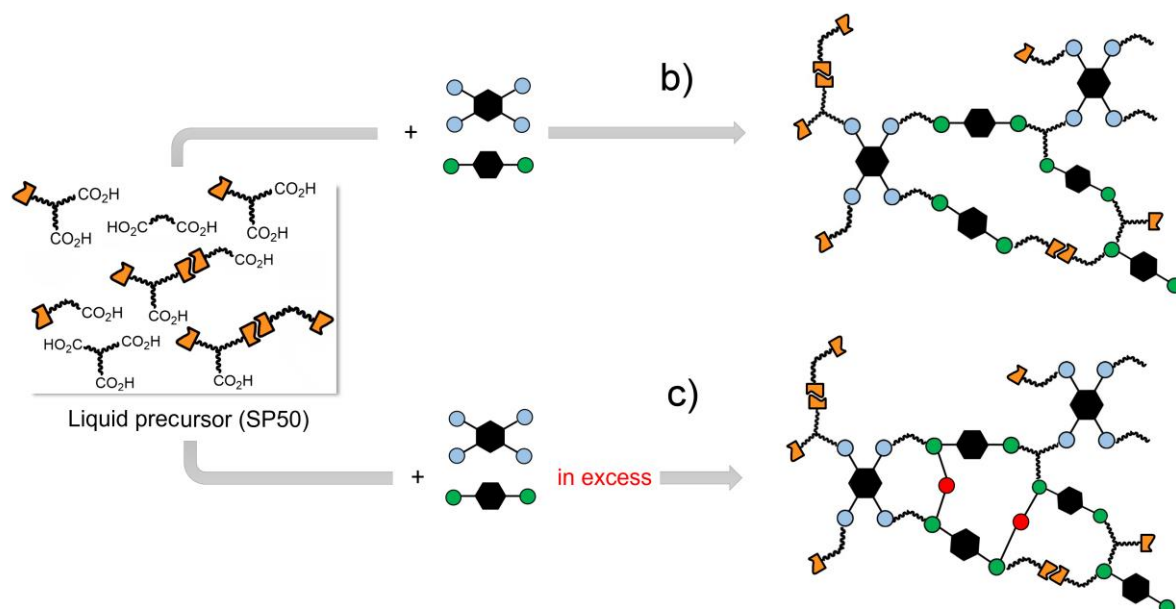
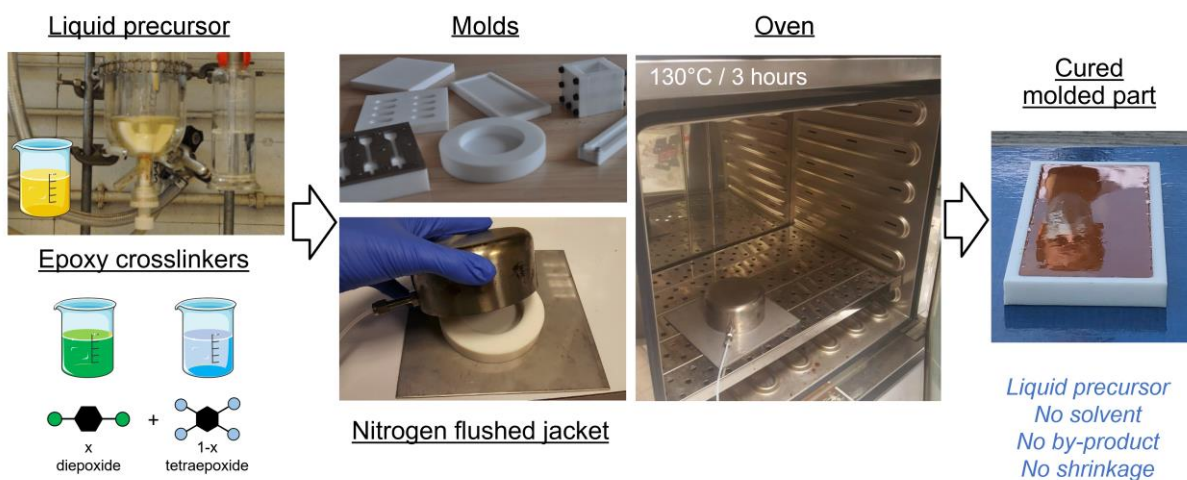


Figure 1. a) Workflow of sample preparation with adjustable quantities of liquid precursor SP50 and epoxy cross-linkers. Illustration of underlying chemical reactions: b) through acid-epoxy addition at 1:1 stoichiometry ($[\text{epoxy}]/[\text{COOH}] = 1$) or c) with involvement of anionic ROP in the presence of an excess of epoxy groups. Red spots represent ether bridges.

2.1 Analysis of the cross-linking reaction

The network formation, which mainly consists in the addition of carboxylic acid functions onto epoxy rings, was monitored by ATR-IR to determine the conversion of both reacting groups. Figure S1a shows the first and last spectrum of 75D-25T_10epoxy with a magnification of the significant peaks in Figure S1b. The carbonyl stretching band at 1710 cm^{-1} is attributed to the carboxylic acid function in the molten state, which shows an intensity decrease during the cross-linking reaction. The ester carbonyl stretching band at 1737 cm^{-1} increases over time,

displaying the expected formation of ester bonds. The disappearance of the epoxy peak (low intensity) at 912 cm^{-1} shows the consumption of epoxy functions even if they are introduced in excess. The integration of these characteristic peaks during the cross-linking reaction is displayed in Figure S1c for the sample 75D-25T_10epoxy. The non-normalized values show the increase of the ester (red circles) and the decline of acid (black squares) and epoxy (blue triangles) peaks initially started with a similar slope. After one hour of cross-linking, the peak integrals stay quite stable which indicates the consumption of all reacting groups. The materials were left for 3 h at $130\text{ }^{\circ}\text{C}$ to ensure the reaction is finished. The difficulty to identify a characteristic band of polyether and the small excess of epoxy functions used in this experiment, both render difficult the analysis of ether bonds formation by IR spectroscopy. However, an increase of an alkyl-aryl ether peak at 1247 cm^{-1} suggests the formation of non-exchangeable ether bonds in the hybrid network. The integration method for this specific peak was confirmed using a test sample containing 50 mol % excess (75D-25T_50epoxy). Peak integrations are shown in Figure S1d with all values normalized by the value of the first peak I_0 . The peak integrals of 75D-25T_10epoxy show a second increase after 50 minutes, which indicates the formation of ether bonds after all COOH groups were consumed. The final plateau is reached after one hour with higher values for an increasing epoxy excess.

The swelling behavior of hybrid networks is shown in Table S2 (images of swollen samples in Figure S2). As expected, the softest composition 75D-25T_0epoxy shows the highest solvent uptake (230 mass %) and soluble fraction (30 mass %), due to the lower number of chemical cross-links in the network. Small epoxy excess (75D-25T_5epoxy, 75D-25T_10epoxy) shows no influence on the solvent uptake (230 mass %) but gives rise to a slightly higher gel content (80 mass %). The few additional ether cross-links have only a small effect on the swelling behavior, as the cross-linking density is only slightly impacted. The formulation containing only tetrafunctional epoxide (0D-100T) exhibits the lowest swelling uptake (130 mass %), in accordance with the high cross-link density of the network.

2.2 Mechanical and thermomechanical properties of the vitrimer materials

Thermomechanical properties of the hybrid network materials were investigated by DSC, DMA and creep analysis.

The glass transition temperature T_g for all compositions was measured by DSC (Table 2 and thermogram curves in Figure S3). For all materials, T_g stands below $20\text{ }^{\circ}\text{C}$, and slightly increases with the excess of epoxy groups, from 12 to $16\text{ }^{\circ}\text{C}$. As expected, the glass transition temperature rises with the cross-link density of the network.

DMA measurements in the film tension mode are presented in Figure S4. Below the glass transition temperature, apparent E' values coarsely match expectation ($> 1\text{ GPa}$). Above $10\text{ }^{\circ}\text{C}$, the storage modulus drops in a same temperature range for all samples. At

high temperatures the storage modulus reaches a plateau which increases with the number of cross-links. The values of E' at 150 °C are reported in Table 2. 75D-25T_0epoxy sample displays the lowest modulus (50 kPa), which rises slightly with excess of epoxy. The material with 100 % TGMDA (0D-100T) displays the highest modulus (0.9 MPa) in accordance to its highly cross-linked network. The dissipation factor, $\tan(\delta)$, shows a broad signal around 50 °C for all compositions, which is commonly associated to network defects such as dangling chains and sol molecules. The signal becomes narrower when the degree of crosslinking increases (see full width at half maximum values of $\tan(\delta)$ peaks in Table 2) which is attributable to a reduction of network defects. Thus, using an excess of epoxy, or changing the ratio of TGMDA are two possible levers to produce materials with tunable damping properties. On the one hand, a high dissipation capacity is useful for reducing contact bounce and improving grip. On the other hand, low dissipation is desirable to enable rapid and repeated tensile motions. Capability to manage the network defects is therefore of prime interest for applications in soft robotics.

Table 2. Glass transition temperature T_g , as measured by DSC. Storage modulus E' as measured by DMA at 150 °C. Full width at half maximum (FWHM) of the $\tan(\delta)$ peak, as measured by DMA. Activation energy of viscosity, tensile stress, and strain at break for the four matrix compositions (standard deviations of three samples minimum from different sheets per composition).

	T_g [°C]	E' (150 °C) [MPa]	FWHM of $\tan(\delta)$ [°C]	Activation energy [kJ/mol]	Maximum stress [MPa]	Maximum strain [%]
0D-100T	16	0.90	45	67	5.6 ± 0.4	143 ± 7
75D-25T_0epoxy	12	0.05	76	55	2.9 ± 0.2	451 ± 26
75D-25T_5epoxy	13	0.06	66	50	3.9 ± 0.1	401 ± 8
75D-25T_10epoxy	16	0.13	57	38	4.3 ± 0.2	333 ± 5

For application in soft robotics, sensor fibers will be integrated in the elastomers. Our sensor fibers being temperature-sensitive, temperature-dependent creep behavior is an interesting feature to test, for evaluation of brazing capability of our composite materials at moderate temperatures. Figure S5 shows the creep behavior of all formulations. The creep results were in turn used to determine η , the viscosity of the materials, according to formula (2):

$$\eta = 100 \times \frac{\sigma}{(\partial \varepsilon / \partial t)} \quad (2)$$

where σ (in Pa) is the applied compressive stress and ε (in % of the initial thickness) the linear strain; the time derivative is measured in the linear portion of the creep curves. The values of viscosity thus determined are plotted in Figure S6, using the Arrhenius representation ($\log_{10}(\eta)$ as a function of $1/T$). For each compound, the data correlate along a straight line, which is characteristic of vitrimers. The plot also enables to measure the activation energy, $E_a = R d(\ln \eta)/d(1/T)$ where R is the ideal gas constant, and to evaluate the topology freezing transition T_v . Customarily, T_v is defined as the temperature below which the viscosity becomes greater than 10^{12} Pa.s, where in practice, flowability is no longer perceptible.¹³

The 0D-100T sample exhibits negligible creep with a maximum deformation of 0.1% after 45 min at 160 °C. The corresponding viscosity approaches the limit values of 10^{11} – 10^{12} Pa.s. Even though the chemical structure is that of a vitrimer, in the absence of a transesterification catalyst, this formulation is physically arrested, showing poor ability to be reshaped in between 110–160 °C. In contrast, 75D-25T_xepoxy samples, which show much lower viscosity (in the range of 10^8 – 10^9 Pa.s) are farther from the transition. 75D-25T_0epoxy (Figure S5b) sample deforms up to 20 % with increasing temperature, indicating good flow properties even at moderately high temperatures. As expected, the off-stoichiometric formulations 75D-25T_5epoxy (Figure S5c) and 75D-25T_10epoxy (Figure S5d) exhibit less creep. However, a linear increase of deformation is still present meaning that a low epoxy excess reduces the creep of the materials without quenching vitrimer properties. The activation energy for each composition was determined from the slope of the Arrhenius plot of viscosity (Table 2). From 75D-25T_0epoxy to 75D-25T_10epoxy, the activation energy decreases with the epoxy excess. Such trend was already observed in previous work²⁶ and was interpreted as the onset of the transition from a vitrimer to a vitrimer-like (more permanent) network.

Tensile tests were conducted to evaluate the mechanical properties at high deformation. One tensile curve per composition is shown in Figure 2 (all curves are presented in Figure S7). The average and standard deviation values of maximum stress and strain are displayed in Table 2. 0D-100T has the highest and 75D-25T_0epoxy the lowest elastic modulus due to the different number of cross-links. The ultimate strength of 75D-25T_5epoxy and 75D-25T_10epoxy increases compared to 75D-25T_0epoxy due to the increased rigidity induced by the additional ether bonds. Interestingly, a slight epoxy excess thus can increase the elastic modulus, keeping suitable creep properties for sensor fiber integration.

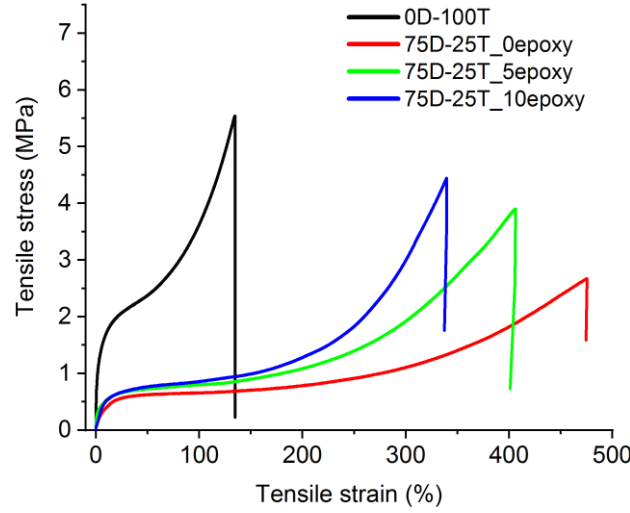


Figure 2. Tensile curves recorded at room temperature at a deformation rate of $25 \text{ mm} \cdot \text{min}^{-1}$ for all matrix compositions.

2.3 Preparation and adhesion of sensor fiber composite (SFC)

For the application in self-healing soft robots, a sensing system is essential to monitor the motions and detect possible damage of the structure. Herein, piezoresistive strain sensor fibers were integrated in the elastomers by a procedure referred as "sandwich-welding" (Figure 3). After the cross-linking step, the thin material sheets were used to punch dog-bone shaped specimens. The sensor was placed between two dog-bone samples, connected to cable wires, and the assembly was pressed for one hour at 80°C (see section 1.5). Composite samples will be identified using a C_prefix in their name.

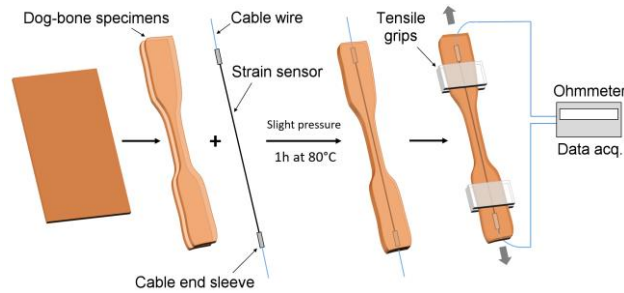


Figure 3. Scheme for the integration of piezoresistive sensor fiber in vitrimer matrix (sandwich-welding). After cross-linking, dog-bone shaped specimens are stamped and sensor fibers are connected to cable wires. Fibers are sandwiched between two dog-bones and sample is welded at 80°C for 1 h.

The quality of the strain sensor integration into the hybrid networks was measured by T-peel tests, as shown in Figure 4. For this experiment, rectangular samples have been prepared to insure a constant surface all along the specimen. As shown by Grande *et al.*,⁴⁵

the initial slope of tensile curves is highly dependent on the stretching speed for these materials, due to the vicinity of T_g . Peeling experiments at $10 \text{ mm} \cdot \text{min}^{-1}$ (Figure S8) showed an overshoot at small deformations and poor stability during the test. Consequently, the peeling speed was reduced to $2.5 \text{ mm} \cdot \text{min}^{-1}$ to ensure elastomeric behavior throughout the test. The C_0D-100T sample exhibits a low peeling strength ($80 \text{ N} \cdot \text{m}^{-1}$), indicating a poor adhesion of both matrix sheets. Conversely, the C_75D-25T_0epoxy sample shows a high peeling strength ($1100 \text{ N} \cdot \text{m}^{-1}$), largely deforming the stretched material and even breaking before delamination (see sample in Figure S9). C_75D-25T_5epoxy and C_75D-25T_10epoxy samples present a high peeling strength around $700 \text{ N} \cdot \text{m}^{-1}$ until delamination. As mentioned above, the epoxy excess provides stiffer networks while keeping creep properties allowing good adhesion ability. Therefore, all C_75D-25T formulations seem suitable for sensor fiber integration, aiming at measuring the material deformation and thus possible damage.

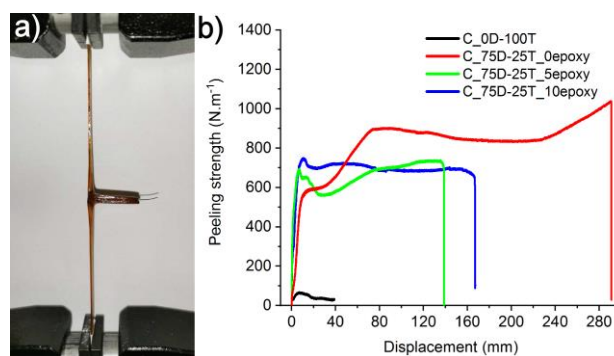


Figure 4. Adhesion measurements: a) T-peel test of a rectangular composite sample (here C_75D-25T_0epoxy) with integrated sensor fiber. b) Peeling strength depending on displacement for the four SFCs (crosshead speed of $2.5 \text{ mm} \cdot \text{min}^{-1}$).

2.4 Mechanical and electrical properties of SFCs

Mechanical and electrical properties of all sensor compositions were analysed simultaneously by tensile tests at large (quasi-static) and short (cyclic) deformations.

Figure 5a shows the stress-strain curve of the network in solid lines and the relative resistance in dotted lines. The ultimate strength is reduced for all materials containing sensor fibers compared to their corresponding matrices (Figure 2). The relative resistance of the integrated fiber increases almost linearly until rupture for all compositions, but the slope for the 0D-100T sample is higher than for the 75D-25T specimens due to a higher stress of the former. As shown by Thurutel *et al.*, the change in relative resistance is determined by the applied strain and stress.³⁷ The poor adhesion properties of 0D-100T composite led to delamination of the samples (Figure 5b). Conversely, the 75D-25T composites present a sharp local breakage (Figure 5c). The relative resistance of the well-integrated strain sensor

shows a similar behavior for the three 75D-25T specimens, with rupture inside the material around 140 % strain, a value suitable for soft robotics applications.

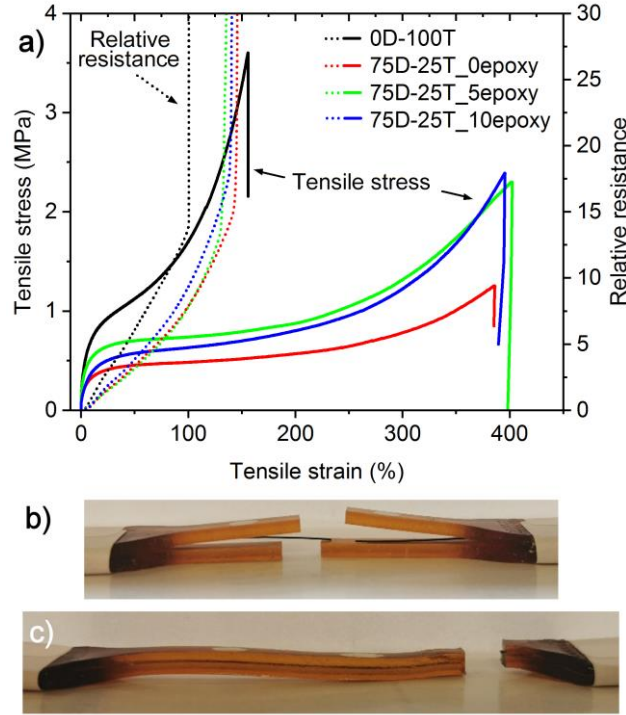


Figure 5. a) Tensile tests of sensor fiber composite at room temperature at a deformation rate of 25 mm.min⁻¹. b) C_0D-100T composite delaminated due to low adhesion matrix-fiber-matrix. c) Sample ruptured locally without delamination (C_75D-25T_0epoxy).

Repeated cyclic tensile displacements are key motions for soft robots. Figure 6 and Figure 7 show the mechanical (solid lines) and electrical (dotted lines) responses of the four SFCs during cycling tests at 0–20 % strain. The maximum stress of C_0D-100T decreases slightly during the cycling (Figure 6a). The plateau at low strain is due to buckling of the sample, when decreasing the crosshead distance just increases the sample bending, without appreciable elastic response. This effect is associated to the nearness of the glass transition temperature, just below room temperature. The piezoresistive strain sensor signal of C_0D-100T shows a positive linear increase of relative resistance with a high amplitude and almost no drift during the cycling. However, due to the poor adhesion of the two matrix moieties, delamination of the sandwich occurred during the cyclic testing (Figure 6b) and the experiment was not repeated after rest.

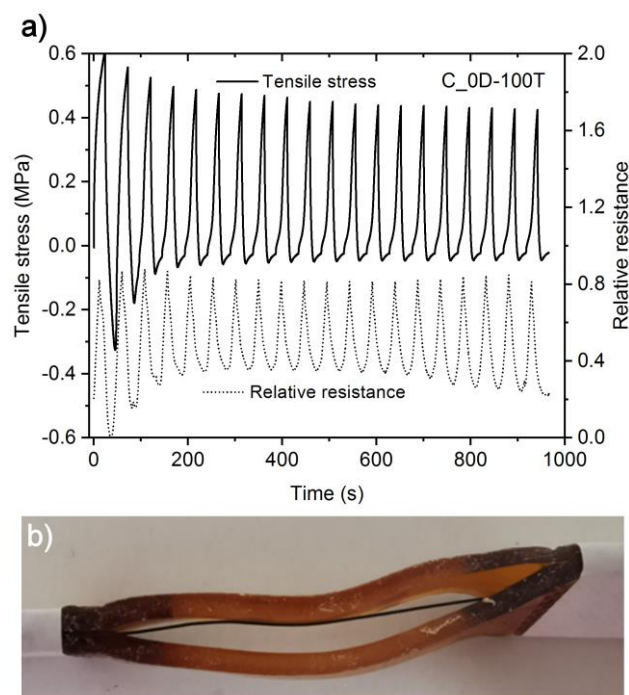


Figure 6. a) Cyclic test (20 cycles of 0–20 % strain) of C_0D-100T composite at room temperature at a deformation rate of 50 %.min⁻¹. b) Delaminated sample after cyclic loading.

For the three C_75D-25T composites at room temperature (Figure 7a-c), the amplitude of both stress and relative resistance decreases over time, in particular at the beginning of the experiment. These effects result from the viscoelastic behavior of the vitrimeric material within each cycle, as the material does not return to its initial length. Consequently, the material undergoes less deformation each cycle, which results in a decreased amplitude of the relative resistance. None of the C_75D-25T samples showed delamination after cyclic loading (representative sample in Figure S10). After two days of rest at room temperature (colored curves in Figure 7a-c), a decrease of the stress amplitude could still be observed, as well as for the pristine samples. Nevertheless, the drift of the relative resistance is lowered, and the response of the strain sensor reaches a plateau after 10 cycles. In practice, several cycles thus could be performed to stabilise and calibrate the sensor before it reaches a stable response for cyclic tests with constant strain.

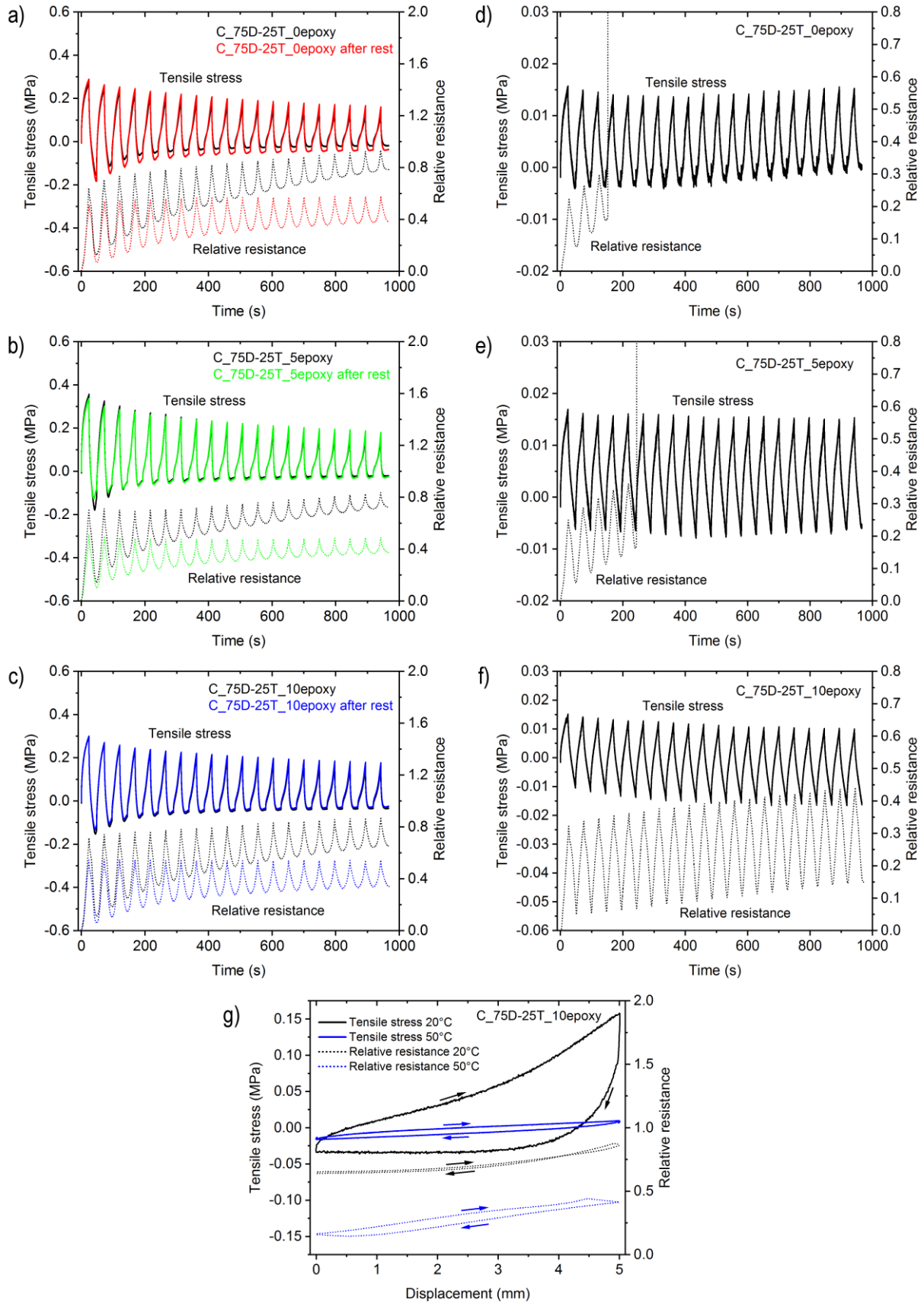


Figure 7. Cyclic tests (20 cycles at 0–20 % strain) for the three C₇₅D-25T SFCs at a deformation rate of 50 %.min⁻¹. Solid lines represent the stress values and dotted lines the relative resistance. Black curves correspond to the pristine samples and colored curves to

the samples after two days of rest. a) C_75D-25T_0epoxy, b) C_75D-25T_5epoxy and c) C_75D-25T_10epoxy tests at room temperature. d) C_75D-25T_0epoxy, e) C_75D-25T_5epoxy and f) C_75D-25T_10epoxy tests at 50 °C. g) Last cycle for C_75D-25T_10epoxy at 20 °C and 50 °C, plotted over displacement.

The same cyclic tensile tests were performed at 50 °C, well above the glass transition temperature of the polymer matrices (Figure 7d-f). Figure 7g shows a representation of the last cycle at 20 °C and 50 °C for the C_75D-25T_10epoxy sample. All C_75D-25T samples exhibit a lower maximum stress and less buckling than at room temperature. Negative stress values originate from the clamping system and the softness of the material, which increases the sample length during cyclic testing. Buckling at room temperature was associated to a large hysteresis of stress, that is strongly reduced when far from the T_g . Conversely, the dependence of the relative resistance on stress³⁷ seems slightly impacted by the temperature. A remarkable difference in the sensor behavior emerges between samples containing 0 % and 5 % epoxy excess (Figure 7d-e) and C_75D-25T_10epoxy composite (Figure 7f). While both first ones exhibit an early rupture of the fiber, after 3 cycles and 5 cycles, respectively, the stiffest sample C_75D-25T_10epoxy responds normally during the whole experiment.

This difference in sensor rupture depending on the epoxy content was further investigated by measuring at 20 °C and 50 °C the Young's moduli of the separate components, the sensor fiber on one side, and the vitrimer matrices on the other side (Figure 8a). The Young's modulus of the matrices was determined by the slope of the first tensile cycle at each temperature. The modulus of the fiber was measured by the slope of a tensile experiment using DMA. At 20 °C, the fiber and the three matrices exhibit relatively comparable Young's moduli.

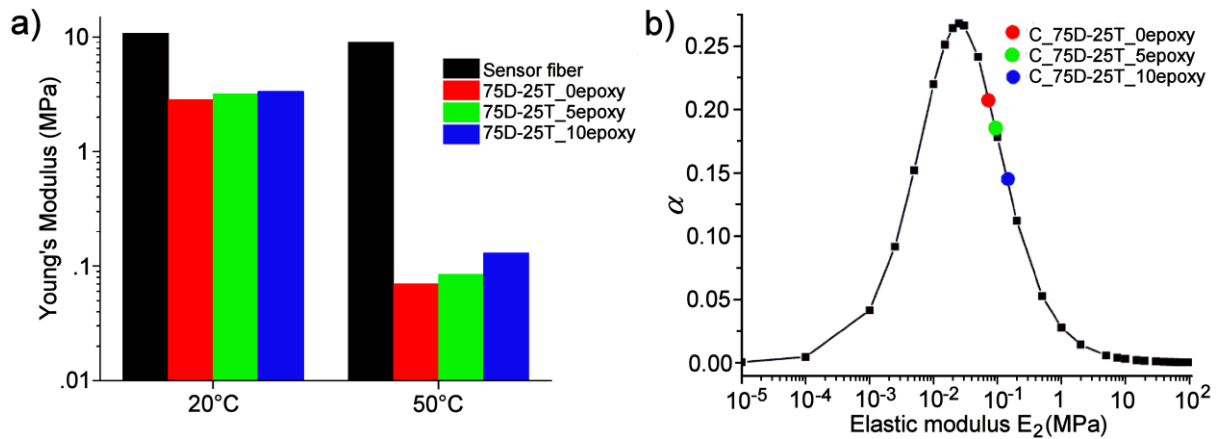


Figure 8. a) Compared Young's moduli of the fiber sensor and the three 75D-25T matrices, at 20 °C and 50 °C. b) Dependence of the ratio $\alpha = \Delta f/f$ at the sensor-matrix interface on E_2 ,

the Young's modulus of the elastomer matrix. $E_1 = 10$ MPa, $S_1 = 0.07$ mm², $S_2 = 16$ mm² and $S'_2 = 48$ mm² (Figure 9g).

However, at 50 °C, more than 30 °C above their T_g , the stiffness of the polymer matrices drops, while the one of the sensor fiber barely decreases. At 20 °C, a rather homogeneous distribution of the tensile stress is expected in the composite because of comparable stiffnesses of fiber and matrix. Conversely, above the T_g of the matrices, the stress distribution may be highly impacted by two factors: not only the difference in Young's moduli of the composite components, but also the dog-bone shape of the composite sample. Indeed, in a tensile bar with varying cross-section, transverse stresses are generated under strain. As described by G'sell in the case of neck formation during bar stretching,⁴⁶ the change of bar section when necking induces local effective stresses in addition to the applied stress. Those stresses may be tensile or compressive, on either side of the inflexion point in the shoulder part (Figure 9a). We investigated if such stress triaxiality in the vicinity of cross-sectional gradients may be at the origine of the early rupture of our fibers, by observations of the dog-bone composite before and after break, under polarized or non polarized light (Figure 9b-f).

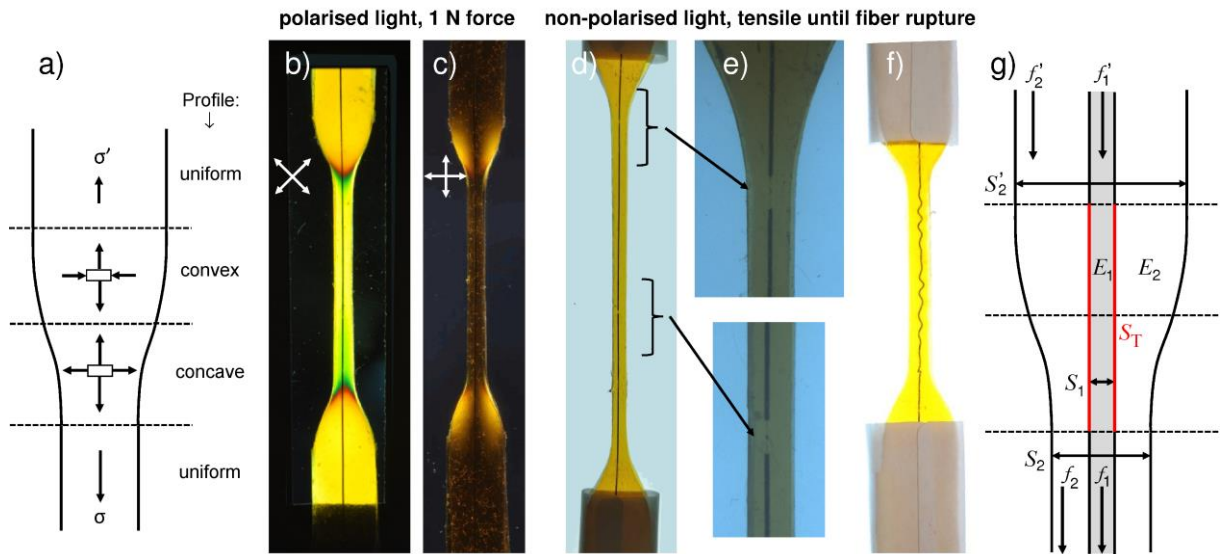


Figure 9. a) Scheme of stress profile (dark arrows) in shoulder region of a dog-bone sample. Bi-axial stress profile in convex (extensive and compressive) and in concave (all tensile) areas. b, c) A SFC sample bearing with 1 N weight observed in polarized light between crossed polarizers oriented at 45° or parallel to the stretching direction. d) Image of stretched C_75D-25T_5epoxy sample showing two spots of fracture of the sensor fiber. e) Zoom-in on the points of rupture observed with a binocular magnifier. f) Broken sample C_75D-25T_5epoxy after relaxation, showing the fiber buckled in the narrow cross-section area. g)

Parameters for calculation of shear stress during stretching: E_1, E_2 , Young's moduli of fiber, matrix, respectively ; S_1, S_2 , cross-sections of fiber, matrix. The projection of fiber-matrix interface S_T is underlined in red ; f_1, f_2 partial strengths applied to fiber, matrix. The (') symbol accounts for parameters in the large part of the specimen.

A force $f = 1$ N was applied to a C_75D-25T_5epoxy sample placed between crossed polarizers. When crossed polarizers are oriented at 45° with respect to the stretching direction, a strong birefringence reflects the stress gradient in both shoulders of the dog-bone (Figure 9b). The darkest line that initiates at both points of inflexion on external sides of the shoulders probably follows the line of strongest stress in the sample. When crossed polarizers are oriented along the stretching direction (Figure 9c), orange quarters appear in both shoulders. The concentration of stress in this region, as pointed out by G'sell *et al.*⁴⁶ in necking cases, is clearly visualized here. In the case of our composite samples, the transverse efforts (extensive and compressive) lead to a stress concentration on the fiber in this region. At the root of the shoulder, in the concave part, stresses are all tensile, causing a phenomenon of cavitation that possibly initiates rupture. The position of the damage in the broken C_75D-25T_5epoxy sample of Figure 7e was observed post-mortem under re-stretch of the dog-bone sample. As observed in Figures 9d and 9e, the fiber was ruptured at two spots, indeed in the root of one shoulder, and also in the central gauge region, where the fiber was not well-centered. After relaxation of the broken sample (Figure 9f), the fiber shows buckling in the area of the narrow cross-section due to the increased stress described above. In these experiments, rupture and buckling of the fiber are induced by a change of shape or a lack of parallelism in the tensile bar, a situation which may be quite representative of robotic parts, whose contours are seldom rectangular.

To describe quantitatively the situation of rupture in our samples, the difference of stiffness between fiber and matrix must be taken into account, in addition to triaxiality effects appearing in the shoulder region. Indeed, as the dog-bone is made of components having different stiffnesses, a shear stress τ is generated all along the interface S_T between fiber and matrix in the shoulder region. τ may be written as the difference of forces Δf applied on the fiber in the narrow (f_1) and large (f'_1) parts divided by the interfacial surface S_T in the shoulder region (Figure 9g):

$$\tau = \frac{\Delta f}{S_T} \quad (3)$$

The overall force f applied to the dog-bone bar may be decomposed into partial forces f_1 and f_2, f'_1 and f'_2 , applied to the fiber and to the matrix, in both extremities of the shoulder:

$$f = f_1 + f_2 = f'_1 + f'_2 \quad (4)$$

and the variation Δf expressed as:

$$\Delta f = f_1 - f'_1 = f_2 - f'_2 \quad (5)$$

Expressing the partial strengths in narrow and large parts of the bar versus their respective strain, surface, modulus, it follows that:

$$\frac{\Delta f}{f} = S_1 E_1 \left(\frac{1}{S_1 E_1 + S_2 E_2} - \frac{1}{S_1 E_1 + S'_2 E_2} \right) = \alpha \quad (6)$$

where α describes the relative variation of the force when the composite sensor is under strain (see calculation details in Supporting Information). Plotting α against E_2 clearly shows that this ratio passes through a maximum value for a Young's modulus of the matrix around 0.025 MPa, and drops rapidly with softer or stiffer matrices (Figure 8b). This extremum corresponds also to a maximum of the shear stress τ . The E_2 values measured for the three matrices at 50 °C were 0.07 MPa, 0.085 MPa and 0.13 MPa for 0 %, 5 %, and 10 % epoxy, respectively. Those matrix moduli may seem quite similar, as compared with the fiber's one, 9 MPa at 50 °C. However, the curve of Figure 8b, where the corresponding α values are indicated, may explain why samples C_75D-25T_0epoxy and _5epoxy broke at 50 °C while C_10epoxy sample did not. Both first ones suffered much more shear stress during cyclic experiments.

Taken the value of interfacial surface $S_T = 9.4 \text{ mm}^2$ in the shoulder area, it comes that the maximum shear stress τ exerted for $f = 1 \text{ N}$ would be around 26 kPa. This relatively low value must be considered in regard of the small strain applied on the dog-bone bar using a 100 g weight. It is also worth to point out that this simple calculation gives rise to an average value on all the interface, without taking into account the localized stress concentrations.

The dog-bone shape of the specimen, useful to apply strong elongation while avoiding break in the clamps, but rather unusual for continuous fiber composites, has underlined the importance of matching the Young's moduli of matrix and fiber. This problem is important to integrate sensors in soft robotics grippers whose shapes are rarely if ever rectangular. This also raises the question of matrix glass temperature. A glass temperature well below room temperature is desirable for improving the mechanical properties of the matrix (faster return, less drift, in particular), but meanwhile possibly worsens the Young's moduli mismatch with a fiber of high modulus. In addition, the analysis of triaxiality in dog-bone shaped specimen may be of interest in experiments involving samples with internal structuration, as for example 3D-printed objects described by Shen *et al.*⁴⁷ These authors showed that the printing angle, *i.e.* the angle between the traveling direction of the nozzle and the long axis of the dog-bone, strongly affects the mechanical properties, especially the

modulus. Triaxiality effects in their dog-bone shaped samples could in addition affect the in-layer and interlayer failure modes.

At least, the stiffest sample C_75D-25T_10epoxy showed fast elastic return at 50 °C and did not break during the 15 first min of cyclic testing, meaning that the contrast of elastic modulus between fiber and matrix may be acceptable for working at a moderately high temperature. Such a composite would thus be suitable for robots operating in warm environments, for instance manipulating in ovens.

Conclusions

In this work, a hybrid network based on the epoxy-acid reaction is synthesized and used to integrate a strain sensor fiber for soft robotics finalities. A sandwich-welding procedure is worked out to encapsulate a sensor fiber between two elastomer strips, merged upon application of heat and pressure. The hybrid network displays advantages such as facile synthesis, tunability of thermo-mechanical properties, vitrimer or vitrimer-like behavior and easy processing for sensor integration.

Network topology is adjusted by varying the ratio diepoxy/tetraepoxy monomers, and by introduction of a small excess of epoxy groups. Hence, the thermo-mechanical properties of the matrix may be managed, allowing for welding at moderate temperature (80 °C) the temperature-sensitive sensor fiber. Moreover, the subsequent good adhesion fiber-matrix avoids premature rupture of the fiber and interfacial delamination of the sandwich composite. The electrical resistance of the sensor increases almost linearly with deformation, and the device breaks at relatively high deformation (140 % strain). The tendency of delamination of the two sandwich moieties strongly depends on matrix stiffness and can be avoided by choosing appropriate composition. Cyclic mechanical and electrical tests at room temperature reveal buckling and drift of the sensor response associated to the vicinity of the glass transition temperature of the matrix (12–16 °C). However, the drift can be reduced with precycling or at larger distance from T_g (50 °C).

The current study shows the interest of using a weldable hybrid network coupled with resistive sensing technology for soft robotics applications, as well as the importance of the Young's moduli matching between sensor fiber and matrix. Current work is in progress to improve the dynamic properties using SH materials based on backbones showing lower T_g values.

Supporting Information.

The Supporting Information is available free of charge at <https://pubs.acs.org/doi/...>

Supramolecular Prepolymer liquid precursor (SP50) preparation (1.2); Hybrid network synthesis (1.3); Quantities of reactants for the preparation of hybrid network sheets (Table S1); Chemical analysis (1.6); Thermomechanical analyses (1.7); ATR-IR spectra (Fig. S1); Solvent uptake and gel content values after immersion in trichlorobenzene for 24 h at 150 °C (Fig. S2 and Table S2); Glass transition temperature T_g of all compositions (Fig. S3); Storage modulus E' and $\tan(\delta)$ from -50 to 200 °C for the four matrix compositions (Fig. S4); Creep measurements for the four matrix compositions (Fig. S5); Arrhenius plots of the viscosities for the four matrix compositions (Fig. S6); Tensile test until rupture for three samples per composition (Fig. S7); Peeling strength depending on displacement for the four SFCs, at a crosshead speed of 10 mm.min⁻¹ (Fig. S8); 75D-25T_0epoxy rectangular sensor fiber sample after rupture of one sheet before delamination (Fig. S9); Representative image of 75D-25T_0epoxy sample after cyclic loading at room temperature with no delamination of matrix sheets (Fig. S10); Calculation of α variation with matrix modulus E_2 .

Acknowledgements. This work was funded by the European Union's Horizon 2020 FET Open Project Self-Healing Soft Robotics [grant agreement No. 828818]. The authors thank ESPCI-PSL, CNRS, EMPA, for supportive financial environment, as well as Arkema for kind gift of UDETA.

References

- [1] Hughes, J.; Culha, U.; Giardina, F.; Guenther, F.; Rosendo, A.; Iida, F. Soft Manipulators and Grippers: A Review. *Front. Robot. AI* **2016**, 3, 69. DOI: [10.3389/frobt.2016.00069](https://doi.org/10.3389/frobt.2016.00069)
- [2] Cianchetti, M.; Laschi, C.; Menciassi, A.; Dario, P. Biomedical Applications of Soft Robotics, *Nat. Rev. Mater.* **2018**, 3, 143–153. DOI: [10.1038/s41578-018-0022-y](https://doi.org/10.1038/s41578-018-0022-y)
- [3] Atalay, A.; Atalay, O.; Husain, M. D.; Fernando, A.; Potluri, P. Piezofilm Yarn Sensor-Integrated Knitted Fabric for Healthcare Applications, *J. Indust. Textiles* **2017**, 47, 505–521. DOI: [10.1177/1528083716652834](https://doi.org/10.1177/1528083716652834)
- [4] Zhang, B.; Xie, Y.; Zhou, J.; Wang, K.; Zhang, Z. State-of-the-Art Robotic Grippers, Grasping and Control Strategies, as well as their Applications in Agricultural Robots: A Review, *Comput. Electron. Agric.* **2020**, 177, 105694. DOI: [10.1016/j.compag.2020.105694](https://doi.org/10.1016/j.compag.2020.105694)
- [5] Pernigoni, L.; Lafont, U.; Grande, A. M. Self-Healing Materials for Space Applications: Overview of Present Development and Major Limitations, *CEAS Space J.* **2021**, 13, 341–352. DOI: [10.1007/s12567-021-00365-5](https://doi.org/10.1007/s12567-021-00365-5)

- [6] Rus, D.; Tolley, M. T. Design, Fabrication and Control of Soft Robots, *Nature* **2015**, 521, 467–475. DOI: [10.1038/nature14543](https://doi.org/10.1038/nature14543)
- [7] Terryn, S.; Langenbach, J.; Roels, E.; Brancart, J.; Bakkali-Hassani, C. ; Poutrel, Q.-A. ; Georgopoulou, A. ; Thuruthel, T. G.; Safaei, A.; Ferrentino, P.; Sebastian, T.; Norvez, S.; Iida, F.; Bosman, A. W.; Tournilhac, F.; Clemens, F.; Van Assche, G.; Vanderborght, B. A Review on Self-Healing Polymers for Soft Robotics, *Materials Today* **2021**, 47, 187–205. DOI: [10.1016/j.mattod.2021.01.009](https://doi.org/10.1016/j.mattod.2021.01.009)
- [8] Terryn, S.; Brancart, J.; Lefeber, D.; Van Assche, G.; Vanderborght, B. Self-Healing Soft Pneumatic Robots, *Sci. Robot.* **2017**, 2, eaan4268. DOI: [10.1126/scirobotics.aan4268](https://doi.org/10.1126/scirobotics.aan4268)
- [9] Cordier, P.; Tournilhac, F.; Soulié-Ziakovic, C.; Leibler, L. Self-Healing and Thermoreversible Rubber from Supramolecular Assembly, *Nature* **2008**, 451, 977–980. DOI: [10.1038/nature06669](https://doi.org/10.1038/nature06669)
- [10] Hoogenboom, R. Hard Autonomous Self-Healing Supramolecular Materials—A Contradiction in Terms? *Angew. Chem. Int. Ed.* **2012**, 51, 11942–11944. DOI: [10.1002/anie.201205226](https://doi.org/10.1002/anie.201205226)
- [11] Zhang, B.; Digby, Z. A.; Flum, J. A.; Foster, E. M.; Sparks, J. L.; Konkolewicz, D. Self-Healing, Malleable and Creep Limiting Materials Using Both Supramolecular and Reversible Covalent Linkages, *Polym. Chem.* **2015**, 6, 7368–7372. DOI: [10.1039/c5py01214g](https://doi.org/10.1039/c5py01214g)
- [12] Neal, J. A.; Mozhdghi, D.; Guan, Z. Enhancing Mechanical Performance of a Covalent Self-Healing Material by Sacrificial Noncovalent Bonds, *J. Am. Chem. Soc.* **2015**, 137, 4846–4850. DOI: [10.1021/jacs.5b01601](https://doi.org/10.1021/jacs.5b01601)
- [13] Montarnal, D.; Capelot, M.; Tournilhac, F.; Leibler, L. Silica-Like Malleable Materials from Permanent Organic Networks, *Science* **2011**, 334, 965–968. DOI: [10.1126/science.1212648](https://doi.org/10.1126/science.1212648)
- [14] Capelot, M.; Montarnal, D.; Tournilhac, F.; Leibler, L. Metal-Catalyzed Transesterification for Healing and Assembling of Thermosets, *J. Am. Chem. Soc.* **2012**, 134, 7664–7667. DOI: [10.1021/ja302894k](https://doi.org/10.1021/ja302894k)
- [15] Capelot, M.; Unterlass, M. M.; Tournilhac, F.; Leibler, L. Catalytic Control of the Vitremer Glass Transition, *ACS Macro Lett.* **2012**, 1, 789–792. DOI: [10.1021/mz300239f](https://doi.org/10.1021/mz300239f)
- [16] Pepels, M.; Pilot, I. A. W.; Klumperman, B.; Goossens, H. Self-Healing Systems Based on Disulfide–Thiol Exchange Reactions, *Polym. Chem.* **2013**, 4, 4955–4965. DOI: [10.1039/C3PY00087G](https://doi.org/10.1039/C3PY00087G)
- [17] Rekondo, A.; Martin, R.; Ruiz de Luzuriaga, A. ; Cabañero, G. ; Grande, H. J. ; Odriozola, I. Catalyst-Free Room-Temperature Self-Healing Elastomers Based on Aromatic Disulfide Metathesis, *Mater. Horiz.* **2014**, 1, 237–240. DOI: [10.1039/C3MH00061C](https://doi.org/10.1039/C3MH00061C)

- [18] Imbernon, L.; Oikonomou, E. K.; Norvez, S.; Leibler, L. Chemically Crosslinked Yet Reprocessable Epoxidized Natural Rubber via Thermo-Activated Disulfide Rearrangements, *Polym. Chem.* **2015**, *6*, 4271–4278. DOI: [10.1039/c5py00459d](https://doi.org/10.1039/c5py00459d)
- [19] Obadia, M. M.; Mudraboyina, B. P.; Serghei, A.; Montarnal, D.; Drockenmuller, E. Reprocessing and Recycling of Highly Cross-Linked Ion-Conducting Networks through Transalkylation Exchanges of C–N Bonds, *J. Am. Chem. Soc.* **2015**, *137*, 6078–6083. DOI: [10.1021/jacs.5b02653](https://doi.org/10.1021/jacs.5b02653)
- [20] Fortman, D. J.; Brutman, J. P.; Cramer, C. J.; Hillmyer, M. A.; Dichtel, W. R. Mechanically Activated, Catalyst-Free Polyhydroxyurethane Vitrimers, *J. Am. Chem. Soc.* **2015**, *137*, 14019–14022. DOI: [10.1021/jacs.5b08084](https://doi.org/10.1021/jacs.5b08084)
- [21] Denissen, W.; Winne, J. M.; Du Prez, F. E. Vitrimers: Permanent Organic Networks with Glass-Like Fluidity, *Chem. Sci.* **2016**, *7*, 30–38. DOI: [10.1039/C5SC02223A](https://doi.org/10.1039/C5SC02223A)
- [22] Röttger, M.; Domenech, T.; van der Weegen, R.; Breuillac, A.; Nicolaÿ, R.; Leibler, L. High-Performance Vitrimers from Commodity Thermoplastics through Dioxaborolane Metathesis, *Science*, **2017**, *356*, 62–65. DOI: [10.1126/science.aah5281](https://doi.org/10.1126/science.aah5281)
- [23] Denissen, W.; De Baere, I.; Van Paepegem, W.; Leibler, L.; Winne, J.; Du Prez, F. E. Vinylogous Urea Vitrimers and Their Application in Fiber Reinforced Composites, *Macromolecules* **2018**, *51*, 2054–2064. DOI: [10.1021/acs.macromol.7b02407](https://doi.org/10.1021/acs.macromol.7b02407)
- [24] Van Zee, N. J.; Nicolaÿ, R. Vitrimers: Permanently Crosslinked Polymers with Dynamic Network Topology, *Prog. Polym. Sci.* **2020**, *104*, 101233. DOI: [10.1016/j.progpolymsci.2020.101233](https://doi.org/10.1016/j.progpolymsci.2020.101233)
- [25] Cash, J. J.; Kubo, T.; Dobbins, D. J.; Sumerlin, B. S. Maximizing the Symbiosis of Static and Dynamic Bonds in Self-Healing Boronic Ester Networks, *Polym. Chem.* **2018**, *9*, 2011–2020. DOI: [10.1039/C8PY00123E](https://doi.org/10.1039/C8PY00123E)
- [26] Poutrel, Q.-A.; Blaker, J. J.; Soutis, C.; Tournilhac, F.; Gresil, M.; Dicarboxylic Acid-Epoxy Vitrimers: Influence of the Off-Stoichiometric Acid Content on Cure Reactions and Thermo-Mechanical Properties, *Polym. Chem.* **2020**, *11*, 5327–5338. DOI: [10.1039/D0PY00342E](https://doi.org/10.1039/D0PY00342E)
- [27] Tangthana-umrung, K.; Poutrel, Q.-A.; Gresil, M. Epoxy Homopolymerization as a Tool to Tune the Thermo-Mechanical Properties and Fracture Toughness of Vitrimers, *asap*, DOI: [10.1021/acs.macromol.1c00861](https://doi.org/10.1021/acs.macromol.1c00861)
- [28] Imbernon, L.; Norvez, S.; Leibler, L. Stress Relaxation and Self-Adhesion of Rubbers with Exchangeable Links, *Macromolecules* **2016**, *49*, 2172–2178. DOI: [10.1021/acs.macromol.5b02751](https://doi.org/10.1021/acs.macromol.5b02751)
- [29] Kaiser, S.; Wurzer, S.; Pilz, G.; Kern, W.; Schlögl, S. Stress Relaxation and Thermally Adaptable Properties in Vitrimer-Like Elastomers from HXNBR Rubber with Covalent Bonds, *Soft Matter*, **2019**, *15*, 6062–6072. DOI: [10.1039/C9SM00856J](https://doi.org/10.1039/C9SM00856J)

- [30] Kaiser, S.; Jandl, J.; Novak, P.; Schlögl, S. Design and Characterisation of Vitrimer-Like Elastomeric Composites from HXNBR Rubber, *Soft Matter* **2020**, *16*, 8577–8590. DOI: [10.1039/d0sm00362j](https://doi.org/10.1039/d0sm00362j)
- [31] Liu, H.; Li, Q.; Zhang, S.; Yin, R.; Liu, X.; He, Y.; Dai, K.; Shan, C.; Guo, J.; Liu, C.; Shen, C.; Wang, X.; Wang, N.; Wang, Z.; Wei, R.; Guo, Z. Electrically Conductive Polymer Composites for Smart Flexible Strain Sensors: a Critical Review, *J. Mater. Chem. C* **2018**, *6*, 12121–12141. DOI: [10.1039/C8TC04079F](https://doi.org/10.1039/C8TC04079F)
- [32] Georgopoulou, A.; Clemens, F. Piezoresistive Elastomer-Based Composite Strain Sensors and Their Applications, *ACS Appl. Electron. Mater.* **2020**, *2*, 1826–1842. DOI: [10.1021/acsaelm.0c00278](https://doi.org/10.1021/acsaelm.0c00278)
- [33] Lu, Y.; Biswas, M. C.; Guo, Z.; Jeon, J.-W.; Wujcik, E. K. Recent Developments in Bio-Monitoring via Advanced Polymer Nanocomposite-Based Wearable Strain Sensors, *Biosensors and Bioelectronics* **2019**, *123*, 167–177. DOI: [10.1016/j.bios.2018.08.037](https://doi.org/10.1016/j.bios.2018.08.037)
- [34] Latif, S.; Amin, S.; Haroon, S. S.; Sajjad, I. A. Self-Healing Materials for Electronic Applications: an Overview, *Mater. Res. Express*. **2019**, *6*, 062001. DOI: [10.1088/2053-1591/ab0f4c](https://doi.org/10.1088/2053-1591/ab0f4c)
- [35] Georgopoulou, A.; Michel, S.; Clemens, F. Sensorized Robotic Skin Based on Piezoresistive Sensor Fiber Composites Produced with Injection Molding of Liquid Silicone, *Polymers* **2021**, *13*, 1226. DOI: [10.3390/polym13081226](https://doi.org/10.3390/polym13081226)
- [36] Georgopoulou, A.; Kummerlöwe, C.; Clemens, F. Effect of the Elastomer Matrix on Thermoplastic Elastomer-Based Strain Sensor Fiber Composites, *Sensors* **2020**, *20*, 2399. DOI: [10.3390/s20082399](https://doi.org/10.3390/s20082399)
- [37] Thuruthel, T. G.; Hughes, J.; Georgopoulou, A.; Clemens, F.; Iida, F. Using Redundant and Disjoint Time-Variant Soft Robotic Sensors for Accurate Static State Estimation, *IEEE Robot. Autom. Lett.* **2021**, *6*, 2099–2105. DOI: [10.1109/LRA.2021.3061399](https://doi.org/10.1109/LRA.2021.3061399)
- [38] Georgopoulou, A.; Michel, S.; Vanderborght, B.; Clemens, F. Piezoresistive Sensor Fiber Composites Based on Silicone Elastomers for the Monitoring of the Position of a Robot Arm, *Sensors and Actuators A: Physical*. **2020**, *318*, 112433. DOI: [10.1016/j.sna.2020.112433](https://doi.org/10.1016/j.sna.2020.112433)
- [39] Sordo, F.; Mougner, S.-J.; Loureiro, N.; Tournilhac, F.; Michaud, V. Design of Self-Healing Supramolecular Rubbers with a Tunable Number of Chemical Cross-Links, *Macromolecules* **2015**, *48*, 4394–4402. DOI: [10.1021/acs.macromol.5b00747](https://doi.org/10.1021/acs.macromol.5b00747)
- [40] Melnykowycz, M.; Koll, B.; Scharf, D.; Clemens, F. Comparison of Piezoresistive Monofilament Polymer Sensors, *Sensors* **2014**, *14*, 1278–1294. DOI: [10.3390/s140101278](https://doi.org/10.3390/s140101278)
- [41] Liu, H.; Li, Q.; Bu, Y.; Zhang, N.; Wang, C.; Pan, C.; Mi, L.; Guo, Z.; Liu, C.; Shen, C.

Stretchable Conductive Nonwoven Fabrics with Self-Cleaning Capability for Tunable Wearable Strain Sensor, *Nano Energy* **2019**, 66, 104143. DOI:

<https://doi.org/10.1016/j.nanoen.2019.104143>

[42] Bu, Y.; Shen, T.; Yang, W.; Yang, S.; Zhao, Y.; Liu, H.; Zheng, Y.; Liu, C.; Shen, C. Ultrasensitive Strain Sensor Based on Superhydrophobic Microcracked Conductive $\text{Ti}_3\text{C}_2\text{T}_x$ MXene/Paper for Human-Motion Monitoring and E-Skin, *Science Bulletin* **2021**, 66, 1849–1857. DOI: <https://doi.org/10.1016/j.scib.2021.04.041>

[43] Moranco, J. M.; Ramis, X.; Fernández-Francos, X.; Konuray, O.; Salla, J. M.; Serra, À. Dual Curing of an Epoxy Resin with Dicarboxylic Acids, *J. Therm. Anal. Calorim.* **2020**, 142, 607–615. DOI: [10.1007/s10973-020-09523-z](https://doi.org/10.1007/s10973-020-09523-z)

[44] Moranco, J. M.; Ramis, X.; Fernández-Francos, X.; Salla, J. M.; Konuray, O.; Serra, À. Curing and Thermomechanical Properties of Off-Stoichiometric Anhydride–Epoxy Thermosets, *Journal of Thermal Analysis and Calorimetry*, *J. Therm. Anal. Calorim.* **2019**, 138, 2865–2872. DOI: [10.1007/s10973-019-08681-z](https://doi.org/10.1007/s10973-019-08681-z)

[45] Grande, A.M.; Garcia, S.J.; van der Zwaag, S. On the Interfacial Healing of a Supramolecular Elastomer, *Polymer* **2015**, 56 (2015) 435–442. DOI: [http://dx.doi.org/10.1016/j.polymer.2014.11.052](https://doi.org/10.1016/j.polymer.2014.11.052)

[46] G'sell, C.; Aly-Helal, N. A.; Jonas, J. J. Effect of Stress Triaxiality on Neck Propagation During the Tensile Stretching of Solid Polymers, *J. Mater. Sci.* **1983**, 18, 1731–1742. DOI: [10.1007/BF00542069](https://doi.org/10.1007/BF00542069)

[47] Shen, N.; Liu, S.; Kasbe, P.; Khabaz, F.; Kennedy, J. P.; Xu, W. Macromolecular Engineering and Additive Manufacturing of Poly(styrene-*b*-isobutylene-*b*-styrene), *ACS Appl. Polym. Mater.* **2021**, 3 (9), 4554–4562. DOI: [10.1021/acsapm.1c00616](https://doi.org/10.1021/acsapm.1c00616)